Seismic characterization of vertical fractures described as general linear-slip interfaces

Vladimir Grechka[⋆], Andrey Bakulin[†] and Ilya Tsvankin[⋆⋆]

[⋆]Center for Wave Phenomena, Department of Geophysics, Colorado School of Mines, Golden, CO 80401-1887, USA (currently at Shell International Exploration and Production Inc., Bellaire Technology Center, 3737 Bellaire Blvd., Houston, TX 77001-0481, USA)

[†]Schlumberger Cambridge Research, High Cross, Madingley Road, Cambridge, CB3 0EL, England (currently at Shell International Exploration and Production Inc., Bellaire Technology Center, 3737 Bellaire Blvd., Houston, TX 77001-0481, USA)

[⋆⋆]Center for Wave Phenomena, Department of Geophysics, Colorado School of Mines, Golden, CO 80401-1887, USA

ABSTRACT

Fluid flow in many hydrocarbon reservoirs is controlled by aligned fractures which make the medium anisotropic on the scale of seismic wavelength. Applying the linear-slip theory, we investigate seismic signatures of the effective medium produced by a single set of "general" vertical fractures embedded in a purely isotropic host rock. The generality of our fracture model means the allowance for coupling between the normal (to the fracture plane) stress and the tangential jump in displacement (and vice versa). Despite its low (triclinic) symmetry, the medium is described by just nine independent effective parameters and possesses several distinct features which help to identify the physical model and estimate the fracture compliances and background velocities. For example, the polarization vector of the vertically propagating fast shear wave S_1 and the semi-major axis of the S_1-wave normal-moveout (NMO) ellipse from a horizontal reflector always point in the direction of the fracture strike. Moreover, for the S_1-wave both the vertical velocity and the NMO velocity along the fractures are equal to the shear-wave velocity in the host rock.

Analysis of seismic signatures in the limit of small fracture weaknesses allows us to select the input data needed for unambiguous fracture characterization. The fracture and background parameters can be estimated using the NMO ellipses from horizontal reflectors and vertical velocities of P-waves and two split S-waves, combined with a portion of the P-wave slowness surface reconstructed from multi-azimuth walkaway VSP (vertical seismic profiling) data. The stability of the parameter-estimation procedure is verified by performing nonlinear inversion based on the exact equations.

Keywords.—fracture characterization, azimuthal anisotropy, wide-azimuth data, moveout inversion, walkaway VSP.

INTRODUCTION

The problem of fracture characterization using seismic data can be divided into two main parts. First, it is necessary to obtain the so-called *effective* model formed by fractures with given micro-structural parameters embedded in a specified host (unfractured) rock. Second, one has to identify the seismic signatures which are sufficiently sensitive to the fracture parameters to ensure a stable inversion procedure.

Effective anisotropic models of fractured formations are usually constructed under the assumption that seismic wavelength is much larger than the fracture openings and the distances between fractures. The existing effective medium theories, treat fractures as surfaces of weakness inside a solid background rock (e.g., Schoenberg 1980, 1983, Hudson 1980, 1981, 1988, Thomsen 1995). Since fractures are small compared to the typical seismic wavelength, it is not surprising that seismic signatures are influenced by certain combinations of various micro-structural fracture parameters rather than by their individual values. Those combinations, called the excess fracture compliances, represent the inherent parameters of the linear-slip theory of Schoenberg (1980, 1983). The compliances effectively absorb such properties of fractures as their shape, interaction, fluid saturation, and the possible presence of pore space hydraulically connected to the fractures (Schoenberg and Douma 1988, Bakulin *et al.* 2000a). Only the compliances can be unambiguously determined from seismic data unless additional information about the microstructural parameters is available.

The linear-slip formalism was shown to be equivalent to several theories which describe fractures in a more deterministic way, as well as to representation of fractures as thin layers of weak anisotropic material (Schoenberg, 1980; Molotkov and Bakulin, 1997). In particular, various models of penny-shaped cracks/contacts (Schoenberg and Douma, 1988; Thomsen 1995; Hudson et al. 1996; Liu et al. 2000) were found to produce an effective medium identical to that of linear slip. Such models were extensively used by Bakulin et al. (2000a) to study the influence of various frac-

ture parameters on seismic signatures. This more deterministic approach, however, requires *a priori* selection of the most suitable fracture model and is currently restricted to a single set of rotationally invariant cracks in a purely isotropic matrix, i.e., to the simplest HTI (transversely isotropic with a horizontal symmetry axis) symmetry. Therefore, treatment of fractures with a more complicated rheology (the topic of this paper) requires application of the general linear-slip theory (Schoenberg and Douma 1988; Schoenberg and Sayers 1995).

Recent advances in the modeling and inversion of wide-azimuth multi-component seismic data helped to make significant progress in solving the second part of the fracture-characterization problem – inverting seismic signatures for the fracture parameters (e.g., Rüger 1997, Rüger and Tsvankin 1997, Tsvankin 1997a, Sayers and Rickett 1997, Contreras *et al.* 1999). In a series of three publications, Bakulin *et al.* (2000a,b,c) described seismic signatures and devised fracture-characterization algorithms for several typical fractured models, from HTI to orthorhombic to monoclinic.

Still, it should be mentioned that while the number of parameters describing the microstructure and microgeometry of fractures can be arbitrarily large (especially, in the presence of multiple fracture sets), the number of the effective stiffness or compliance coefficients is limited to 21 for the most general triclinic anisotropy. Thus, it is clear that only a limited subset of fractured models is uniquely constrained by seismic data. A simple example of ambiguity in fracture characterization is presented by Bakulin *et al.* (2002), who show that the compliances of two vertical orthogonal fracture sets embedded in a VTI (transversely isotropic with a vertical symmetry axis) background cannot be resolved from the effective stiffnesses.

Here, we examine the effective medium produced by the most general (in terms of the linear-slip theory) parallel vertical fractures in a purely isotropic host rock. In contrast to the conventional treatment of fractures in effective medium theory, our model accounts for coupling between the *normal* (to the fracture plane) stress and *tangential* jump in displacement (and vice versa). This coupling may be caused by

at least two different physical mechanisms – micro-corrugation of fracture faces or misalignment between the fracture strike and the principal axes of stress. The first mechanism, proposed by Schoenberg and Douma (1988), was employed by Bakulin *et al.* (2000c) to study fluid-dependent shear-wave splitting observed on field data by Guest *et al.* (1998). The existence of the second mechanism was confirmed by physical experiments of Nakagawa *et al.* (2000), who investigated reflections from fractures subjected to stresses which principal directions deviated from the fracture strike.

Although the model produced by the "general" fracture set has the lowest possible symmetry (triclinic), it is described by the fracture orientation and only *eight* independent parameters, which facilitates the development of fracture-characterization methods based on seismic data. To study the influence of fractures on the kinematics of P- and S-waves, we derive weak-anisotropy approximations linearized in the fracture weaknesses. The analytic results also help to devise a stable fracture-characterization algorithm based on the combination of reflection and VSP (vertical seismic profiling) data.

EFFECTIVE MODEL OF A GENERAL FRACTURE SET

We consider a single system of parallel vertical fractures embedded in an otherwise isotropic host rock. According to the linear-slip theory of Schoenberg (1980, 1983), the effective compliance $\boldsymbol{s}$ of such a medium in the low-frequency limit is simply the sum of the background compliance $\boldsymbol{s}_b$ and the excess fracture compliance $\boldsymbol{s}_f$:

$$\boldsymbol{s} = \boldsymbol{s}_b + \boldsymbol{s}_f \,, \tag{1}$$

where $\boldsymbol{s}$, $\boldsymbol{s}_b$, and $\boldsymbol{s}_f$ are 6×6 symmetric, non-negative definite matrices.

Excess fracture compliance

For a single set of vertical fractures with the normals parallel to the x_1-axis, the excess compliance $\boldsymbol{s}_f$ is given by (Schoenberg 1980)

$$\boldsymbol{s}_f = \begin{pmatrix} K_N & 0\ 0\ 0 & K_{NV} & K_{NH} \\ 0 & 0\ 0\ 0 & 0 & 0 \\ 0 & 0\ 0\ 0 & 0 & 0 \\ 0 & 0\ 0\ 0 & 0 & 0 \\ K_{NV} & 0\ 0\ 0 & K_V & K_{VH} \\ K_{NH} & 0\ 0\ 0 & K_{VH} & K_H \end{pmatrix} . \tag{2}$$

The compliances K_N, K_V, K_H, K_{NV}, K_{NH} and K_{VH} appear in the boundary conditions of the so-called linear slip which relate the jumps in displacement (or slips) $[\boldsymbol{u}] = \{[u_1], [u_2], [u_3]\}^T$ across the fracture plane to the traction (stress) components $\boldsymbol{T} = \{\sigma_{11}, \sigma_{12}, \sigma_{13}\}^T$ (Schoenberg 1980, Molotkov and Bakulin 1997):

$$[\boldsymbol{u}] = h\, \boldsymbol{K}\, \boldsymbol{T} . \tag{3}$$

Here h is the average distance (spacing) between the fractures, and

$$\boldsymbol{K} \equiv \begin{pmatrix} K_N & K_{NV} & K_{NH} \\ K_{NV} & K_V & K_{VH} \\ K_{NH} & K_{VH} & K_H \end{pmatrix} . \tag{4}$$

Note that while the linear-slip theory assumes the traction to be continuous across the fractures, some theoretical models (not considered here) lead to a discontinuity in traction (Tod and Hudson 2001).

The physical meaning of the compliances in equations (3) and (4) is discussed in detail in the literature (e.g., Schoenberg and Douma 1988, Berg *et al.* 1991, Schoenberg and Sayers 1995, Schoenberg and Helbig 1997, Bakulin *et al.* 2000a,c). Usually fractures are assumed to be rotationally invariant with the compliances satisfying the conditions of Schoenberg and Sayers (1995):

$$K_V = K_H , \tag{5}$$

$$K_{NV} = K_{NH} = K_{VH} = 0 . \tag{6}$$

Several publications (e.g., Schoenberg and Helbig 1997, Bakulin *et al.* 2000b) treat fractures which are *not* invariant with respect to rotation but are still described by a diagonal compliance matrix [i.e., they obey the constraint (6), but $K_V \neq K_H$]. It is clear from equation (3) that the off-diagonal elements K_{NV}, K_{NH}, K_{VH} of the matrix (4) are responsible for the coupling between the traction normal to the fracture plane and tangential slip (and vice versa); the mechanisms responsible for such coupling are discussed in the introduction.

Dry and fluid-filled fractures

Here it is appropriate to discuss the criteria needed to distinguish between dry and fluid-filled fractures. Schoenberg and Sayers (1995) established such criteria for rotationally invariant fractures which satisfy the conditions (5) and (6). Based on the experiments of Hsu and Schoenberg (1993) and Pyrak-Nolte *et al.* (1990a,b), they suggested to use the ratio K_N/K_V as an indicator of fluid content. According to Schoenberg and Sayers (1995),

$$\frac{K_N}{K_V} \approx 1 \quad \text{or} \quad K_N \approx K_V \tag{7}$$

for dry fractures, and

$$\frac{K_N}{K_V} \approx 0 \quad \text{or} \quad K_N \approx 0 \tag{8}$$

for fractures saturated with fluid. As shown by Bakulin *et al.* (2000a), equations (7) and (8) can also be derived from Hudson's (1980) theory for isolated penny-shaped cracks.

Bakulin *et al.* (2000c) extended the criteria (7) and (8) to micro-corrugated fractures, for which $K_{NV} \neq 0$, but

$$K_{NH} = K_{VH} = 0\,. \tag{9}$$

They considered the eigenvalues $\tilde{\Lambda}_1$ and $\tilde{\Lambda}_2$ of the 2×2 submatrix

$$\tilde{\boldsymbol{K}} = \begin{pmatrix} K_N & K_{NV} \\ K_{NV} & K_V \end{pmatrix} \tag{10}$$

of matrix (4) and stated that in their model $\tilde{\Lambda}_1$ and $\tilde{\Lambda}_2$ play the role of K_N and K_V. Therefore, for dry fractures

$$\tilde{\Lambda}_1 \approx \tilde{\Lambda}_2 \,, \tag{11}$$

and for fluid-filled fractures

$$\min\left(\tilde{\Lambda}_1,\, \tilde{\Lambda}_2\right) \approx 0 \,. \tag{12}$$

Here, we further generalize the criteria (11) and (12) for fractures with non-zero compliances K_{NH}, K_{VH} and K_{NV} using the eigenvalues Λ_1, Λ_2, and Λ_3 of the full compliance matrix $\boldsymbol{K}$ [equation (4)]. By analogy with equations (11) and (12), dry fractures are supposed to be approximately equally compliant in all three principal directions, which means that

$$\Lambda_1 \approx \Lambda_2 \approx \Lambda_3 \,. \tag{13}$$

In contrast, isolated fluid-filled fractures should be much less compliant in the direction which corresponds to squeezing the fluid. Hence,

$$\min\left(\Lambda_1,\, \Lambda_2,\, \Lambda_3\right) \approx 0. \tag{14}$$

The criteria (13) and (14) are used in the discussion of numerical examples below.

Properties of the stiffness matrix

To obtain the compliance matrix $\boldsymbol{s}$ of the effective medium, we substitute equation (2) and the compliance of the isotropic background [e.g., equation (2) of Bakulin et al. (2000c)] into equation (1):

$$\boldsymbol{s} = \begin{pmatrix} \dfrac{\lambda+\mu}{\mu(3\lambda+2\mu)} + K_N & \dfrac{-\lambda}{2\mu(3\lambda+2\mu)} & \dfrac{-\lambda}{2\mu(3\lambda+2\mu)} & 0 & K_{NV} & K_{NH} \\ \dfrac{-\lambda}{2\mu(3\lambda+2\mu)} & \dfrac{\lambda+\mu}{\mu(3\lambda+2\mu)} & \dfrac{-\lambda}{2\mu(3\lambda+2\mu)} & 0 & 0 & 0 \\ \dfrac{-\lambda}{2\mu(3\lambda+2\mu)} & \dfrac{-\lambda}{2\mu(3\lambda+2\mu)} & \dfrac{\lambda+\mu}{\mu(3\lambda+2\mu)} & 0 & 0 & 0 \\ 0 & 0 & 0 & \dfrac{1}{\mu} & 0 & 0 \\ K_{NV} & 0 & 0 & 0 & \dfrac{1}{\mu} + K_V & K_{VH} \\ K_{NH} & 0 & 0 & 0 & K_{VH} & \dfrac{1}{\mu} + K_H \end{pmatrix}, \quad (15)$$

where λ and μ are the Lamé constants of the background. Then, the effective stiffness matrix $\boldsymbol{c} = \boldsymbol{s}^{-1}$ takes the form

$$\boldsymbol{c} = \left(\begin{array}{ccc|c|cc} c_{11} & \chi\, c_{11} & \chi\, c_{11} & 0 & c_{15} & c_{16} \\ \chi\, c_{11} & c_{22} & c_{23} & 0 & \chi\, c_{15} & \chi\, c_{16} \\ \chi\, c_{11} & c_{23} & c_{22} & 0 & \chi\, c_{15} & \chi\, c_{16} \\ \hline 0 & 0 & 0 & c_{44} & 0 & 0 \\ \hline c_{15} & \chi\, c_{15} & \chi\, c_{15} & 0 & c_{55} & c_{56} \\ c_{16} & \chi\, c_{16} & \chi\, c_{16} & 0 & c_{56} & c_{66} \end{array}\right); \quad (16)$$

$$\chi \equiv \frac{\lambda}{\lambda + 2\,\mu}\,. \quad (17)$$

Although this matrix formally corresponds to the lowest possible symmetry (triclinic), it describes a special type of triclinic media defined by less than 21 independent stiffness elements. Indeed, five components of the matrix (16) are equal to zero, while other stiffnesses satisfy the following relationships:

$$c_{12} = c_{13} = \chi\, c_{11}\,, \quad c_{22} = c_{33}\,, \quad c_{25} = c_{35} = \chi\, c_{15} \quad \text{and} \quad c_{26} = c_{36} = \chi\, c_{16}\,. \quad (18)$$

In addition, there are two more constraints on the effective stiffnesses:

$$c_{22} = \chi\, c_{12} + 2\,(1+\chi)\, c_{44} \quad (19)$$

and

$$c_{22} = c_{23} + 2\,c_{44}\,. \tag{20}$$

Equation (20), rewritten as

$$c_{13}\,(c_{22} + c_{12}) = c_{23}\,(c_{11} + c_{12})\,, \tag{21}$$

coincides with a constraint obtained by Schoenberg and Helbig (1997) for fracture-induced orthorhombic anisotropy.

Equations (18)–(20) indicate that only eight combinations of the sixteen nonzero stiffness coefficients in equation (16) are independent. The same conclusion follows from the fact that the matrix $\boldsymbol{c}$ is constructed from two parameters of the isotropic host rock (λ and μ) and six excess fracture compliances (K_N, K_V, K_H, K_{NV}, K_{NH} and K_{VH}). Thus, the effective model of the most general vertical fracture set is defined by the fracture orientation and eight independent elastic parameters.

Note that the compliance and stiffness matrices can be divided into several blocks marked by the solid lines in equation (16). In particular, the only non-zero element of the block that includes the elements of the fourth column and the fourth row is c_{44} for $\boldsymbol{c}$ and s_{44} for $\boldsymbol{s}$. Since $s_{44} = 1/\mu$, the inversion of the compliance matrix yields

$$c_{44} = s_{44}^{-1} = \mu\,. \tag{22}$$

As discussed below, equation (22) has important implications for fracture-characterization algorithms operating with seismic data.

Effective stiffness coefficients in the weak-anisotropy limit

Definition of weaknesses.—It is convenient to replace the fracture compliances by the dimensionless *weaknesses* defined for the diagonal elements of the compliance matrix as (Hsu and Schoenberg 1993, Bakulin *et al.* 2000a)

$$\Delta_N \equiv \frac{(\lambda + 2\,\mu)\,K_N}{1 + (\lambda + 2\,\mu)\,K_N}\,, \tag{23}$$

$$\Delta_V \equiv \frac{\mu\, K_V}{1+\mu\, K_V}\,, \tag{24}$$

$$\Delta_H \equiv \frac{\mu\, K_H}{1+\mu\, K_H}\,. \tag{25}$$

Similarly, for the off-diagonal compliances we can introduce the weaknesses in the following way:

$$\Delta_{NV} \equiv \frac{\sqrt{\mu\,(\lambda+2\,\mu)}\, K_{NV}}{1+\sqrt{\mu\,(\lambda+2\,\mu)}\, K_{NV}}\,, \tag{26}$$

$$\Delta_{NH} \equiv \frac{\sqrt{\mu\,(\lambda+2\,\mu)}\, K_{NH}}{1+\sqrt{\mu\,(\lambda+2\,\mu)}\, K_{NH}}\,, \tag{27}$$

$$\Delta_{VH} \equiv \frac{\sqrt{\mu\,(\lambda+2\,\mu)}\, K_{VH}}{1+\sqrt{\mu\,(\lambda+2\,\mu)}\, K_{VH}}\,. \tag{28}$$

Note that for the special case of penny-shaped cracks, the weaknesses are proportional to the *crack density* defined as the number of cracks per unit volume multiplied with their cubed largest semi-axis (Schoenberg and Douma 1988, Bakulin *et al.* 2000a). Since the matrix (4) of the excess compliances is non-negative definite, the weaknesses Δ_N, Δ_V and Δ_H vary from zero to unity. The vanishing weaknesses imply the absence of fractures, while the values $\Delta_N = 1$, $\Delta_V = 1$ or $\Delta_H = 1$ are indicative of an extreme degree of fracturing, with the velocities of P- or S-waves across the fractures going to zero. In addition, the stability condition that requires the matrix (4) to be non-negative definite leads to the following inequalities (written for the leading-order terms in the weaknesses)

$$\Delta_{NV}^2 \le \Delta_N\, \Delta_V\,, \quad \Delta_{NH}^2 \le \Delta_N\, \Delta_H\,, \quad \text{and} \quad \Delta_{VH}^2 \le \Delta_V\, \Delta_H\,. \tag{29}$$

Linearized expressions for the stiffnesses.—To gain insight into the influence of the fractures on the effective stiffnesses, it is convenient to expand the matrix $\boldsymbol{c}$ in the weaknesses and truncate the expansion after the linear terms. The resulting linearized expressions are valid for weaknesses much smaller than unity (i.e., for a weakly anisotropic effective medium):

$$\Delta_N \ll 1\,, \quad \Delta_V \ll 1\,, \quad \Delta_H \ll 1\,,$$

$$|\,\Delta_{NV}\,| \ll 1\,, \quad |\,\Delta_{NH}\,| \ll 1\,, \quad |\,\Delta_{VH}\,| \ll 1\,. \tag{30}$$

To derive the approximate stiffness matrix, we express the fracture compliances through the weaknesses using equations (23)–(28) and substitute them into the effective compliance matrix $\boldsymbol{s}$ [equation (15)]. Then the stiffness coefficients are found by inverting $\boldsymbol{s}$ and dropping all quadratic and higher-order terms in the weaknesses:

$$c_{11} \approx (\lambda + 2\,\mu)\,(1 - \Delta_N)\,, \tag{31}$$

$$c_{12} = c_{13} \approx \lambda\,(1 - \Delta_N)\,, \tag{32}$$

$$c_{15} \approx -\Delta_{NV}\,\sqrt{\mu\,(\lambda + 2\,\mu)}\,, \tag{33}$$

$$c_{16} \approx -\Delta_{NH}\,\sqrt{\mu\,(\lambda + 2\,\mu)}\,, \tag{34}$$

$$c_{22} = c_{33} \approx (\lambda + 2\,\mu)\left[1 - \Delta_N\,\chi^2\right]\,, \tag{35}$$

$$c_{23} \approx \lambda\,(1 - \Delta_N\,\chi)\,, \tag{36}$$

$$c_{25} = c_{35} \approx -\Delta_{NV}\,\sqrt{\lambda\,\mu\,\chi}\,, \tag{37}$$

$$c_{26} = c_{36} \approx -\Delta_{NH}\,\sqrt{\lambda\,\mu\,\chi}\,, \tag{38}$$

$$c_{44} = \mu\,, \tag{39}$$

$$c_{55} \approx \mu\,(1 - \Delta_V)\,, \tag{40}$$

$$c_{56} \approx -\Delta_{VH}\,\mu\,\sqrt{\frac{\mu}{\lambda + 2\,\mu}}\,, \tag{41}$$

$$c_{66} \approx \mu\,(1 - \Delta_H)\,, \tag{42}$$

where χ is given by equation (17). Equations (31)–(42) provide the basis for developing linearized expressions for seismic signatures in the next section.

Special cases.—If the weaknesses Δ_{NH} and Δ_{VH} vanish, the effective medium becomes monoclinic with the symmetry plane $[x_1,\, x_3]$. Bakulin *et al.* (2000c) showed that this result, which follows from equations (34), (38), and (41), is exact (i.e., it is not limited to small weaknesses).

If the excess compliance matrix (4) is diagonal [see equation (6)] and

$$\Delta_{NV} = \Delta_{NH} = \Delta_{VH} = 0\,, \tag{43}$$

the symmetry becomes orthorhombic. A more complicated model of this type composed of parallel vertical fracture set in an anisotropic (VTI) background was examined by Schoenberg and Helbig (1997) and Bakulin *et al.* (2000b).

If, in addition to equation (43), we assume equal tangential compliances,

$$K_V = K_H \quad \text{or} \quad \Delta_V = \Delta_H\,, \tag{44}$$

the fractures become rotationally invariant (Schoenberg and Sayers 1995). In this case, the medium is transversely isotropic with the symmetry axis pointing in the x_1-direction (HTI). Seismic fracture-characterization methods for HTI media are discussed in Bakulin *et al.* (2000a).

Contribution of the off-diagonal weakness elements.—Equations (31)–(42) clearly indicate that the weaknesses Δ_{NV}, Δ_{NH} and Δ_{VH} have a first-order influence only on the off-diagonal stiffness components c_{ij} with either i or j equal to 5 or 6. According to the results of Grechka *et al.* (2000), this implies that the vertical velocities and semi-major axes of pure-mode NMO ellipses from horizontal reflectors should be close to those in orthorhombic media described by a diagonal compliance matrix [equations (43)]. The non-zero weaknesses Δ_{NV}, Δ_{NH}, and Δ_{VH}, however, should cause a *rotation* of the NMO ellipses of different modes with respect to each other, similar to that discussed by Grechka *et al.* (2000) for monoclinic media with a horizontal symmetry plane. Below, we give analytic description of the velocities, NMO ellipses and slowness surfaces for the fracture-induced triclinic medium.

SEISMIC VELOCITIES AND SLOWNESSES FOR GENERAL FRACTURES

Here, we present linearized expressions for the vertical velocities and NMO ellipses of P-, S_1- and S_2-waves and for the slowness surface of P-waves. The goal of employing

approximations is to identify the seismic signatures needed to constrain different fracture weaknesses. The closed-form expressions given here also yield the Frechét derivatives of the seismic signatures with respect to the fracture parameters, which can be used to guide nonlinear inversion based on the exact equations.

Phase velocities of *P*- and *S*-waves in the fracture plane [x_2, x_3]

First, we derive the phase velocities V_P, V_{S1}, and V_{S2} of P- and two split S-waves for propagation in the vertical plane [x_2, x_3]. The phase velocity V of a plane wave traveling in the direction $\boldsymbol{n} = [\,0,\, n_2,\, n_3\,]$ can be obtained from the Christoffel equation,

$$\det(c_{ijkl}\, n_j\, n_k - \rho\, V^2\, \delta_{il}) = 0\,. \tag{45}$$

Here c_{ijkl} is the stiffness tensor represented in matrix form in equation (16), and δ_{il} is Kronecker's symbolic delta. Summation from 1 to 3 over repeated indices is implied.

Taking into account the constraints (18)–(20), equation (45) in the [x_2, x_3]-plane becomes

$$\begin{aligned}\left[c_{44} - \rho\, V^2\right] \Big[\left(c_{33} - \rho\, V^2\right)\left(c_{55}\, n_3^2 + 2\, c_{56}\, n_2\, n_3 + c_{66}\, n_2^2 - \rho\, V^2\right) - \\ - \left(c_{26}^2\, n_2^2 + 2\, c_{25}\, c_{26}\, n_2\, n_3 + c_{25}^2\, n_3^2\right)\Big] = 0\,.\end{aligned} \tag{46}$$

Hence, the equation for phase velocity reduces to the product of two terms. The first term describes a pure SV-wave with the polarization vector $\boldsymbol{A}^{SV} = [0,\, -n_3,\, n_2]$ that lies in the [x_2, x_3]-plane perpendicular to the propagation vector $\boldsymbol{n} = [\,0,\, n_2,\, n_3\,]$. The velocity of the SV-wave is independent of angle and equal to the shear-wave velocity in the background:

$$V_{SV} = \sqrt{\frac{c_{44}}{\rho}} = \sqrt{\frac{\mu}{\rho}} = V_{Sb}\,. \tag{47}$$

Below we show that the velocity of the second shear wave in the [x_2, x_3]-plane is always smaller than V_{Sb}, so the SV-wave represents the faster shear mode S_1. The "isotropic"

behavior of the S_1-wave in the fracture plane follows from the constraints (18)–(20) on the stiffness elements. In particular, the equalities $c_{22} = c_{33}$ and $c_{22} = c_{23} + 2\,c_{44}$ would imply vanishing anisotropic coefficients ϵ and δ in VTI media and in the symmetry plane $[x_2,\, x_3]$ of orthorhombic media (Tsvankin 1997b, 2001).

The velocities of the P-wave and second S-wave will be derived in the limit of small weaknesses [see the inequalities (30)]. Using the approximations for the relevant stiffness coefficients [equations (31)–(42)] in equation (46) and ignoring the terms containing c_{25}^2, c_{26}^2, and $c_{25}\,c_{26}$ (they are quadratic with respect to the weaknesses) yields

$$V_P \approx \sqrt{\frac{c_{33}}{\rho}} \approx V_{Pb}\,\left(1 - \frac{\Delta_N}{2}\,\chi^2\right)\,, \tag{48}$$

$$\begin{aligned} V_{S2} \;&\approx \sqrt{\frac{c_{55}\,n_3^2 + 2\,c_{56}\,n_2\,n_3 + c_{66}\,n_2^2}{\rho}} \\ &\approx V_{Sb}\,\left[1 - \frac{1}{2}\left(\Delta_H\,n_2^2 + 2\,\frac{V_{Sb}}{V_{Pb}}\,\Delta_{VH}\,n_2\,n_3 + \Delta_V\,n_3^2\right)\right]\,. \end{aligned} \tag{49}$$

Equation (48) shows that the P-wave velocity for small weaknesses does not change with angle, but is different from the background velocity. The velocity variation (49) of the second shear wave S_2 resembles that of the SH-wave in transversely isotropic media (the slowness surface of the SH-wave is elliptical). Since the weaknesses Δ_V and Δ_H are non-negative and $\Delta_{VH}^2 \le \Delta_V\,\Delta_H$ [equation (29)], it can inferred from equation (49) that $V_{S2} \le V_{Sb}$, or $V_{S2} \le V_{SV}$. Therefore, the SV-wave is indeed the faster shear mode in the $[x_2,\, x_3]$-plane:

$$V_{SV} \equiv V_{S1} \ge V_{S2}\,. \tag{50}$$

The velocities of S_1- and S_2-waves at vertical incidence $\boldsymbol{n} = [0,\, 0,\, 1]$ are

$$V_{S1,0} = V_{Sb} \tag{51}$$

and

$$V_{S2,0} \approx V_{Sb}\left(1 - \frac{\Delta_V}{2}\right). \tag{52}$$

The approximate vertical velocities of P- and S_2-waves depend on just two weaknesses – Δ_N and Δ_V. As a result, all three vertical velocities have exactly the same form as those for rotationally invariant fractures in an isotropic background (Schoenberg and Sayers 1995, Bakulin *et al.* 2000a).

Equations (51) and (52) allow us to obtain the shear-wave splitting coefficient at vertical incidence:

$$\gamma^{(S)} \equiv \frac{V_{S1,0}^2 - V_{S2}^2, 0}{2\,V_{S2,0}^2} \approx \frac{\Delta_V}{2}\,, \tag{53}$$

Again, the linearized expression (53) for the splitting coefficient coincides with that for less general fracture sets (e.g., Schoenberg and Sayers 1995, Schoenberg and Helbig 1997, Bakulin *et al.* 2000a,b). A more accurate approximation for $\gamma^{(S)}$ (containing quadratic terms in the weaknesses) reveals that the shear-wave splitting coefficient depends on the off-diagonal weaknesses and, therefore, is influenced by the type of fracture infill (Bakulin *et al.* 2000c). Note that for rotationally invariant penny-shaped cracks with $\Delta_{NV} = \Delta_{NH} = \Delta_{VH} = 0$, $\gamma^{(S)}$ is approximately equal to the crack density (e.g., Schoenberg and Douma 1988, Tsvankin 1997a).

It should be emphasized that while equations (52), (53), and inequality (50) were derived under the assumption of small weaknesses, the above results for the fast mode S_1 (SV) are exact. For any magnitude of the weaknesses, the polarization vector of the S_1-wave is confined to the fracture plane, and the velocity V_{S1} coincides with that of the host rock. The same results were obtained by Bakulin *et al.* (2000a,b,c) for models containing one set of rotationally invariant vertical fractures.

NMO ellipses from a horizontal reflector

Azimuthally varying normal-moveout (NMO) velocity of any pure-mode reflected wave is described by a simple quadratic form (Grechka and Tsvankin 1998),

$$V_{\rm nmo}^{-2}(\alpha) = W_{11}\cos^2\alpha + 2\,W_{12}\sin\alpha\cos\alpha + W_{22}\sin^2\alpha\,, \tag{54}$$

where α is the azimuth measured with respect to the x_1-axis. Equation (54) can be applied for arbitrarily anisotropic, heterogeneous media, provided reflection moveout on conventional-spread common-midpoint (CMP) gathers is sufficiently close to hyperbolic. If the CMP traveltime increases with offset for all azimuthal directions (which is usually the case), $V_{\rm nmo}(\alpha)$ traces out an ellipse in the horizontal plane.

For a homogeneous horizontal layer, the matrix $\boldsymbol{W}$ has the following form (Grechka, Tsvankin and Cohen 1999):

$$\boldsymbol{W} = \frac{q}{q_{,12}^2 - q_{,11}q_{,22}} \begin{pmatrix} q_{,22} & -q_{,12} \\ -q_{,12} & q_{,11} \end{pmatrix}, \tag{55}$$

where q is the vertical component of the slowness vector $\boldsymbol{p} = [\,p_1,\, p_2,\, q\,]$ of the zero-offset ray, and $q_{,ij} \equiv \partial^2 q(p_1,\, p_2)/(\partial p_i \partial p_j)$; the derivatives should be evaluated for the zero-offset ray. For a horizontal reflector, the slowness vector of the zero-offset reflection is vertical, i.e., $\boldsymbol{p} = [\,0,\, 0,\, q\,]$.

The vertical slowness q and its derivatives with respect to the horizontal slownesses can be found from the Christoffel equation (45) which allows us to express the matrices $\boldsymbol{W}$ from equation (55) through the stiffness coefficients. [An approximate expression for the vertical slowness of P-waves is given in equation (65) below.] Then the linearized stiffnesses from equations (31)–(42), along with the vertical slownesses reciprocal to the vertical velocities (48), (51), and (52), are substituted into equation (55). Further linearization of the matrices $\boldsymbol{W}$ in the fracture weaknesses gives

$$\boldsymbol{W}^P \approx \frac{1}{V_{Pb}^2} \begin{pmatrix} 1 + \Delta_N\,(1 - 4\,g_b^2) + 4\,\Delta_V\,g_b & 2\,\Delta_{NH}\,(1 - 2\,g_b)\,\sqrt{g_b} \\ 2\,\Delta_{NH}\,(1 - 2\,g_b)\,\sqrt{g_b} & 1 + \Delta_N\,(1 - 2\,g_b)^2 \end{pmatrix}, \tag{56}$$

$$\boldsymbol{W}^{S1} \approx \frac{1}{V_{S\,b}^2} \begin{pmatrix} 1 + \Delta_H - \dfrac{\Delta_{VH}^2}{\Delta_V}\, g_b & 0 \\ 0 & 1 \end{pmatrix}, \tag{57}$$

$$\boldsymbol{W}^{S2} \approx \frac{1}{V_{S\,b}^2} \begin{pmatrix} 1 - 3\,\Delta_V + 4\,g_b\,\Delta_N + \dfrac{\Delta_{VH}^2}{\Delta_V}\, g_b & 2\,\Delta_{NH}\,\sqrt{g_b} \\ 2\,\Delta_{NH}\,\sqrt{g_b} & 1 + \Delta_H \end{pmatrix}; \tag{58}$$

$$g_b \equiv \left(\frac{V_{Sb}}{V_{Pb}}\right)^2. \tag{59}$$

The approximations for the vertical velocities and NMO ellipses of reflected waves help to evaluate the feasibility of estimating the fracture weaknesses and the background parameters from seismic data. Several observations of particular importance to the inversion procedure are listed below.

1. None of the linearized equations (48), (51), (52), (56)–(58) contains the weakness Δ_{NV}. Hence, the vertical and NMO velocities are not sensitive enough to Δ_{NV} and cannot be used to estimate this parameter.

2. The weakness Δ_{VH} appears only in the expressions for W_{11}^{S1} and W_{11}^{S2} as part of the combination $g_b\,\Delta_{VH}^2/\Delta_V$. [This combination does not become infinite when $\Delta_V \to 0$ because, according to the third inequality (29), $\Delta_{VH}^2/\Delta_V < \Delta_H$.] Even though the ratio Δ_{VH}^2/Δ_V can be considered linear in the weakness Δ_{VH}, the weighting factor g_b is too small for Δ_{VH} to be tightly constrained by the shear-wave NMO ellipses.

3. The weighting factors for the weaknesses Δ_N, Δ_V, Δ_H, and Δ_{NH} in equations (56)–(58) range from $2\,\sqrt{g_b}$ ($2\,\sqrt{g_b} \approx 1$ for a common vertical-velocity ratio of 0.5) to 3. This suggests that the inversion of the vertical velocities and NMO ellipses for those four weaknesses should be sufficiently stable. Below, we support this conclusion by numerical tests.

4. Although the matrix $\boldsymbol{W}^{S1}$ [equation (57)] was derived in the limit of small weaknesses, the expressions for its elements W_{12}^{S1} and W_{22}^{S1} are exact:

$$W_{12}^{S1} = W_{21}^{S1} = 0\,, \tag{60}$$

and

$$W_{22}^{S1} = \frac{1}{V_{S_b}^2} = \frac{1}{V_{S1}^2}\,. \tag{61}$$

This result follows from the fact that the velocity of the S_1-wave does not change with angle within the fracture plane [x_2, x_3]. The physical meaning of equations (60) and (61) is clear: irrespective of the magnitude of the fracture weaknesses, the semi-major axis of the S_1-wave NMO ellipse is parallel to the fracture strike, and the NMO velocity in the fracture plane is equal to the vertical velocity of the S_1-wave. Thus, if we can measure both the vertical velocity V_{S1} and the NMO ellipse $\boldsymbol{W}^{S1}$ of the fast S-wave, equation (61) can be used to verify whether or not the underlying physical model (i.e., a single set of vertical fractures in an isotropic background) is correct. The presence of either anisotropy in the background or a second fracture system will cause a difference between the NMO velocity of the S_1-wave in the fracture direction and the vertical velocity V_{S1}.

An example of the pure-mode NMO ellipses in a horizontal layer with fractures which can be considered as "almost" dry [$\Lambda_1 = 0.12$, $\Lambda_2 = 0.15$, and $\Lambda_3 = 0.18$, see equation (13)] is given in Fig. 1. As predicted by the analytic results above, the NMO ellipse of the S_1-wave (thick solid line) is co-oriented with the fractures, and its semi-major axis is parallel to the fracture strike (the azimuth $\alpha = 90^\circ$). While the semi-major axis of the P-wave NMO ellipse points approximately in the same direction ($\alpha = 89^\circ$), for the slow S_2-wave the azimuth of the semi-major axis $\alpha = -11^\circ$, which is close to the normal to the fractures.

The misalignment of the NMO ellipses proved its usefulness for anisotropic parameter estimation in monoclinic media (Grechka *et al.* 2000), and we expect it to give information about the weakness Δ_{NH} [equations (56) and (58)]. Note that the NMO velocity of the slow (S_2) shear wave in Fig. 1 is *greater* than that of the fast (S_1) wave for a wide range of azimuths ($-30^\circ < \alpha < 30^\circ$). Such a behavior of shear-wave NMO ellipses is not necessarily indicative of a low anisotropic symmetry because it was observed by Grechka, Theophanis and Tsvankin (1999) in a physical-modeling experiment for the higher-symmetry orthorhombic (phenolic) material.

P-wave slowness surface

According to the above results, the vertical and NMO velocities of the three pure-mode reflections do not constrain the weaknesses Δ_{NV} and Δ_{VH}. A potentially useful source of information about Δ_{NV} and Δ_{VH} is multi-azimuth walkaway VSP data which can be used to reconstruct a portion of the P-wave slowness surface

$$q \equiv q(p_1, p_2)\,; \tag{62}$$

q, as before, is the vertical slowness component, and p_1 and p_2 are the horizontal slownesses. Our goal here is to examine the function $q(p_1, p_2)$ and study the possibility of inverting it for Δ_{NV} and Δ_{VH}.

If the fracture weaknesses [x_2, x_3]-plane are small, the differences

$$\boldsymbol{c}^{\Delta} = \boldsymbol{c} - \boldsymbol{c}_b \tag{63}$$

between the effective and background stiffness coefficients [equations (16), (31)–(42)] also become small quantities of the same order. A general approximation for q in arbitrary anisotropic media, linearized in the perturbations of the stiffness elements, has the form

$$q \approx q_b - \frac{1}{\rho}\left\{ \frac{1}{2\,q_b}\left(p_1^4\, c_{11}^{\Delta} + p_2^4\, c_{22}^{\Delta} + q_b^4\, c_{33}^{\Delta}\right)\right.$$

$$+\frac{1}{q_b}\left[p_1^2\,p_2^2\,\left(c_{12}^{\Delta}+2\,c_{66}^{\Delta}\right)+p_1^2\,q_b^2\,\left(c_{13}^{\Delta}+2\,c_{55}^{\Delta}\right)+p_2^2\,q_b^2\,\left(c_{23}^{\Delta}+2\,c_{44}^{\Delta}\right)\right]$$

$$+2\,p_1\,p_2\left[p_1\left(c_{14}^{\Delta}+2\,c_{56}^{\Delta}\right)+p_2\left(c_{25}^{\Delta}+2\,c_{46}^{\Delta}\right)+q_b\left(c_{36}^{\Delta}+2\,c_{45}^{\Delta}\right)\right] \tag{64}$$

$$+2\,p_1\left(p_1^2\,c_{15}^{\Delta}+q_b^2\,c_{35}^{\Delta}\right)+2\,p_2\left(p_2^2\,c_{24}^{\Delta}+q_b^2\,c_{34}^{\Delta}\right)+2\,\frac{p_1\,p_2}{q_b}\left(p_1^2\,c_{16}^{\Delta}+p_2^2\,c_{26}^{\Delta}\right)\Bigg\}.$$

Taking into account that for the model at hand $c_{14}^{\Delta}=c_{24}^{\Delta}=c_{34}^{\Delta}=c_{45}^{\Delta}=c_{46}^{\Delta}=0$ and using the linearized expressions (31)–(42) for the stiffnesses, we find

$$\begin{aligned} q \approx q_b &+\frac{1}{q_b}\left[\frac{(\nu-2\,g_b)^2}{2\,V_{Pb}^2}\,\Delta_N+2\,p_1^2\,V_{S\,b}^2\left(p_2^2\,\Delta_H+q_b^2\,\Delta_V\right)\right] \\ &+2\,p_1\,\sqrt{g_b}\left[(\nu-2\,g_b)\left(\Delta_{NV}+\frac{p_2}{q_b}\,\Delta_{NH}\right)+2\,p_1\,p_2\,V_{S\,b}^2\,\Delta_{VH}\right]. \end{aligned} \tag{65}$$

Here

$$q_b=\sqrt{\frac{1}{V_{Pb}^2}-p_1^2-p_2^2} \tag{66}$$

is the vertical slowness in the isotropic host rock, and

$$\nu\equiv 1-2\,p_1^2\,V_{S\,b}^2\,. \tag{67}$$

Equation (65) explains the structure of the matrix $\boldsymbol{W}^P$ (i.e., the P-wave NMO ellipse) [equation (56)] that depends on the vertical slowness and its second derivatives with respect to the horizontal slownesses p_1 and p_2 for $p_1=p_2=0$. In particular, note that the weaknesses Δ_{NV} and Δ_{VH} in equation (65) are multiplied with *odd* powers of p_i and, therefore, do not contribute to the matrix $\boldsymbol{W}^P$.

Clearly, the presence of Δ_{NV} and Δ_{VH} makes the P-wave slowness surface $q(p_1,p_2)$ asymmetric with respect to the vertical slowness direction $p_1=p_2=0$ and also with respect to the horizontal plane $q=0$. This asymmetry, however, has no influence on pure-mode reflection traveltimes, as long as the reflector is horizontal. Therefore,

not only the NMO ellipse, but also long-spread P-wave moveout from horizontal interfaces is independent of the weaknesses Δ_{NV} and Δ_{VH}. In contrast, multi-azimuth walkaway VSP data can be used to reconstruct the slowness surface for both positive and negative p_i and possibly estimate Δ_{NV} and Δ_{VH}.

Figures 2 and 3 confirm that the slowness surface $q(p_1, p_2)$ is not an even function of p_1 and p_2. As follows from equation (65), the asymmetry with respect to the slowness component p_1 (governed by the weakness Δ_{NV}) is more pronounced than that with respect to p_2, especially for small horizontal slownesses. The shift of the maximum of the curve $q(p_1)$ toward positive p_1 in Fig. 3 is correctly predicted by the linearized approximation (65).

FRACTURE CHARACTERIZATION

The analytic results above, obtained in the limit of small fracture weaknesses, suggest that the vertical velocities and NMO ellipses of P-, S_1- and S_2-waves from a horizontal reflector constrain all background and fracture parameters except for the weaknesses Δ_{NV} and Δ_{VH}. Adding P-wave multi-azimuth walkaway VSP data can help to estimate Δ_{NV} and Δ_{VH} using a near-vertical portion of the P-wave slowness surface. Those preliminary conclusions are supported below by the actual nonlinear inversion for the fracture and background parameters.

Inversion of the vertical velocities and NMO ellipses

Suppose the fractured layer is horizontal and sufficiently thick for measuring the interval NMO ellipses of P-, S_1- and S_2-waves with acceptable accuracy. If pure shear-wave reflections are not excited, their traveltimes can be reconstructed from 3-D multi-azimuth P-wave and converted-wave (PS_1 and PS_2) reflection data using the methodology of Grechka and Tsvankin (2002). Application of 3-D semblance velocity analysis (Grechka and Tsvankin 1999) then produces the NMO ellipses of the pure modes S_1 and S_2.

Velocity analysis of split shear waves should be preceded by Alford (1986) rotation designed to identify the S-wave polarization directions and separate the fast and slow modes. Since the fracture azimuth coincides with the polarization vector of the fast wave S_1, it can be found prior to the inversion procedure. We can refine the estimate of the fracture direction and check the validity of our model after obtaining the S_1-wave NMO ellipse, whose semi-major axis should be aligned with the fractures. In the tests below it is assumed that the fracture orientation has already been found, and the velocity information should be inverted for the background parameters and fracture weaknesses.

Figure 4 shows the inversion results for the model used in Figs. 1 and 2. The input data include the vertical velocities of P-, S_1- and S_2-waves and their NMO ellipses (i.e., the matrices $\boldsymbol{W}$) from a horizontal reflector. The error bars in Fig. 4 are caused by Gaussian noise added to the vertical velocities (with the standard deviation 0.5%) and the matrices $\boldsymbol{W}$ (with the standard deviation 2%). The results give a clear confirmation of our analytic predictions based on the assumption of small weaknesses.[1] The confidence intervals for the V_S/V_P ratio in the background and the weaknesses Δ_N, Δ_V, Δ_H and Δ_{NH} do not exceed 0.03, which is not much higher than the relative magnitude of the noise added to the NMO ellipses. In contrast, the error bars for Δ_{NV} and Δ_{VH} reach ± 0.2; evidently, those weaknesses are poorly constrained by the data.

The above conclusions remain practically unchanged for an effective medium formed by fluid-filled fractures (Fig. 5). The estimates of g_b, Δ_N, Δ_V, Δ_H and Δ_{NH} are quite stable with respect to errors in the input data, while the inversion for Δ_{NV} and Δ_{VH} requires additional information.

---

[1]Note that the fracture weaknesses in this model are not small. Estimating the crack density from the shear-wave splitting coefficient [equation (53)], as is usually done for penny-shaped cracks, gives a value of 12.5%.

Inversion of the *P*-wave slowness surface

Next, we examine whether or not the P-wave slowness surface provides sufficient information for constraining the weaknesses Δ_{NV} and Δ_{VH}. The results shown in Fig. 6 are obtained for the model from Fig. 4 by inverting for Δ_{NV} and Δ_{VH} the portion of the P-wave slowness surface displayed in Fig. 2. The parameters g_b, Δ_N, Δ_V, Δ_H and Δ_{NH} are fixed at the values estimated from the vertical velocities and NMO ellipses. The error bars for the weaknesses Δ_{NV} and Δ_{VH} in Fig. 6 are associated with both the errors in the other model parameters (taken from Fig. 4) and Gaussian noise with the standard deviation 2% added to the P-wave vertical slowness $q(p_1, p_2)$.

Comparison of Figs. 6 and 4 shows that including the P-wave slowness surface makes the inversion for Δ_{NV} and Δ_{VH} much more stable. Still, while the confidence interval for Δ_{NV} is similar to that for the diagonal weaknesses, the error bar for Δ_{VH} is about twice as large. This result is not surprising because the near-vertical segment of the P-wave slowness surface is more sensitive to Δ_{NV} than it is to Δ_{VH} [see equation (65]. A similar reduction in the error bars for Δ_{NV} and Δ_{VH} after the inversion of the P-wave slowness surface is observed for fluid-filled fractures (compare Figs. 7 and 5).

It seems that the vertical and NMO velocities may not be needed at all for estimating the fracture parameters because the P-wave slowness surface alone depends on all six weaknesses [equation (65)]. Numerical tests indicate, however, that such an inversion produces less stable results than those in Figs. 6 and 7, most likely because of the trade-offs between the model parameters and the limited range of the horizontal slownesses p_1 and p_2 available in VSP surveys.

DISCUSSION AND CONCLUSIONS

A set of parallel vertical fractures of the most general (in terms of the linear-slip theory) type embedded in otherwise isotropic host rock produces an effective medium of triclinic symmetry. Whereas triclinic media depend on up to 21 stiffness coeffi-

cients, such a model is fully defined by the fracture azimuth and just eight independent parameters – the background coefficients λ and μ and six fracture compliances (or weaknesses). The relative simplicity of this fracture-induced triclinic anisotropy [see the stiffness matrix (16)] suggests that the background and fracture parameters can be found from the effective stiffness elements. The two key issues in fracture characterization, however, are how to establish the symmetry of the model and develop a stable and efficient methodology for recovering the stiffnesses from seismic data.

Our analysis reveals several distinctive signatures of the effective medium which may help to identify the underlying physical model. First, both the polarization vector of the vertically traveling fast shear wave S_1 and the semi-major axis of the S_1-wave NMO ellipse from a horizontal reflector are parallel to the fractures, while the NMO ellipses of the P- and S_2-waves have different orientations. Second, the vertical velocity of the S_1-wave and its NMO velocity in the fracture plane are equal to each other and to the shear-wave velocity in the host rock. The S_1-wave does not have such properties in models with multiple fracture sets or anisotropy in the background rock (Bakulin *et al.* 2000b,c).

To study the influence of fractures on seismic signatures, we expressed the velocities, slownesses and NMO ellipses of P-waves and split S-waves directly through the fracture weaknesses using the weak-anisotropy approximation (i.e., in the limit of small weaknesses). The analytic results show that the fracture orientation, the weaknesses Δ_N, Δ_V, Δ_H and Δ_{NH}, and the background velocities V_{Pb} and V_{Sb} can be estimated from the vertical velocities of P-, S_1- and S_2-waves and their NMO ellipses from a horizontal reflector. It should be emphasized that it is possible to reconstruct the NMO ellipses of pure shear reflections from P- and PS-wave 3-D multi-azimuth reflection data, so shear-wave excitation is not necessary (Grechka and Tsvankin 2002). The two remaining weaknesses, Δ_{NV} and Δ_{VH}, can be obtained by inverting the P-wave slowness surface measured in multi-azimuth walkaway VSP surveys.

The analytic results served as a guide to the inversion procedure based on the exact equations. Numerical tests confirm that the combination of three different types of seismic data (the vertical velocities and NMO ellipses of pure-mode reflections and the P-wave slowness surface measured by VSP) constrains the fracture weaknesses needed for a robust solution of the fracture-characterization problem. The uncertainties in five inverted weaknesses (all except for Δ_{VH}) are close to the errors introduced in the input data. It is likely that a more accurate estimate of Δ_{VH} can be obtained by increasing the range of incidence angles (horizontal slownesses) used for computing the P-wave slowness surface.

Given the importance of fracture networks for fluid flow in hydrocarbon reservoirs, the methodology described here should find a number of applications in reservoir characterization. We demonstrated that the inversion of multicomponent wide-azimuth seismic data can be used to find the orientation and weaknesses (or compliances) of vertical fractures with general rheology embedded in an isotropic host rock. The six-element weakness matrix can be used to map "sweet spots" of intense fracturing and to discriminate between dry and fluid-filled fracture systems.

ACKNOWLEDGMENTS

We are grateful to members of the A(nisotropy)-Team of the Center for Wave Phenomena (CWP), Colorado School of Mines, for helpful discussions. Reviews by Ken Larner (CSM), Phil Christie, Henk Keers and Chris Chapman (all of Schlumberger) helped to improve the manuscript. V. Grechka and I. Tsvankin were supported by the Consortium Project on Seismic Inverse Methods for Complex Structures at CWP and by the Chemical Sciences, Geosciences and Biosciences Division, Office of Basic Energy Sciences, U.S. Department of Energy.

REFERENCES

Alford R.M. 1986. Shear data in the presence of azimuthal anisotropy. 56th SEG meeting, Expanded Abstracts, 476–479.

Bakulin A., Grechka V. and Tsvankin I. 2000a. Estimation of fracture parameters from reflection seismic data. Part I: HTI model due to a single fracture set. *Geophysics* **65**, 1788–1802.

Bakulin A., Grechka V. and Tsvankin I. 2000b. Estimation of fracture parameters from reflection seismic data. Part II: Fractured models with orthorhombic symmetry. *Geophysics* **65**, 1803–1817.

Bakulin A., Grechka V. and Tsvankin I. 2000c. Estimation of fracture parameters from reflection seismic data. Part III: Fractured models with monoclinic symmetry. *Geophysics* **65**, 1818–1830.

Bakulin A., Grechka V. and Tsvankin I. 2002. Seismic inversion for the parameters of two orthogonal fracture sets in a VTI background medium. *Geophysics* **67**, 292–299.

Berg E., Hood J. and Fryer G. 1991. Reduction of the general fracture compliance matrix Z to only five independent elements. *Geophysical Journal International* **107**, 703–707.

Contreras P., Grechka V. and Tsvankin I. 1999. Moveout inversion of P-wave data for horizontal transverse isotropy. *Geophysics* **64**, 1219–1229.

Grechka V., Contreras P. and Tsvankin I. 2000. Inversion of normal moveout for monoclinic media. *Geophysical Prospecting* **48**, 577–602.

Grechka V., Theophanis S. and Tsvankin I. 1999. Joint inversion of P- and PS-waves in orthorhombic media: Theory and a physical-modeling study. *Geophysics* **64**,

146–161.

Grechka V. and Tsvankin I. 1998. 3-D description of normal moveout in anisotropic media. *Geophysics* **63**, 1079–1092.

Grechka V. and Tsvankin I. 1999. 3-D moveout inversion in azimuthally anisotropic media with lateral velocity variation: Theory and a case study. *Geophysics* **64**, 1202–1218.

Grechka, V. and Tsvankin I. 2002. $PP + PS = SS$. *Geophysics* **67**, 1961–1971.

Grechka V., Tsvankin I. and Cohen J.K. 1999. Generalized Dix equation and analytic treatment of normal-moveout velocity for anisotropic media: *Geophysical Prospecting* **47**, 117–148.

Guest S., van der Kolk C. and Potters H. 1998. The effect of fracture filling fluids on shear-wave propagation. 68th SEG meeting, Expanded Abstracts, 948–951.

Hudson J.A. 1980. Overall properties of a cracked solid. *Mathematical Proceedings of the Cambridge Philosophical Society* **88**, 371–384.

Hudson J.A. 1981. Wave speeds and attenuation of elastic waves in material containing cracks. *Geophysical Journal of the Royal Astronomical Society* **64**, 133–150.

Hudson J.A. 1988. Seismic wave propagation through material containing partially saturated cracks. *Geophysical Journal* **92**, 33–37.

Hudson J.A., Liu E. and Crampin S. 1996. Transmission properties of a plane fault. *Geophysical Journal International* **125**, 559–566.

Hsu C.-J. and Schoenberg M. 1993. Elastic waves through a simulated fractured medium. *Geophysics* **58**, 964–977.

Liu E., Hudson J.A. and Pointer T. 2000. Equivalent medium representation of fractured rock. *Journal of Geophysical Research* **105**, No. B2, 2981–3000.

Molotkov L.A. and Bakulin A.V. 1997. An effective model of a fractured medium with fractures modeled by the surfaces of discontinuity of displacements. *Journal of Mathematical Sciences* **86**, No. 3, 2735–2746.

Nakagawa S., Nihei K.T. and Myer L.R. 2000. Shear-induced conversion of seismic wave across single fractures. *International Journal of Rock Mechanics and Mining Sciences* **37**, No. 1-2, 203–218.

Pyrak-Nolte L.J., Myer L.R. and Cook N.G.W. 1990a. Transmission of seismic waves across single natural fractures. *Journal of Geophysical Research* **95(B6)**, 8617–8638.

Pyrak-Nolte L.J., Myer L.R. and Cook N.G.W. 1990b. Anisotropy in seismic velocities and amplitudes from multiple parallel fractures. *Journal of Geophysical Research* **95(B7)**, 11345–11358.

Rüger A. 1997. *P*-wave reflection coefficients for transversely isotropic models with vertical and horizontal axis of symmetry. *Geophysics* **62**, 713–722.

Rüger A. and Tsvankin I. 1997. Using AVO for fracture detection: Analytic basis and practical solutions. *The Leading Edge* **10**, 1429–1434.

Sayers C. and Rickett J.E. 1997. Azimuthal variation in AVO response for fractured gas sands. *Geophysical Prospecting* **45**, 165–182.

Schoenberg M. 1980. Elastic wave behavior across linear slip interfaces. *Journal of Acoustical Society of America* **68**, 1516–1521.

Schoenberg M. 1983. Reflection of elastic waves from periodically stratified media with interfacial slip. *Geophysical Prospecting* **31**, 265–292.

Schoenberg M. and Douma J. 1988. Elastic wave propagation in media with parallel fractures and aligned cracks. *Geophysical Prospecting* **36**, 571–590.

Schoenberg M. and Helbig K. 1997. Orthorhombic media: Modeling elastic wave behavior in a vertically fractured earth. *Geophysics* **62**, 1954–1974.

Schoenberg M. and Sayers C. 1995. Seismic anisotropy of fractured rock. *Geophysics* **60**, 204–211.

Thomsen L. 1995. Elastic anisotropy due to aligned cracks in porous rock. *Geophysical Prospecting* **43**, 805–830.

Tod S.R. and Hudson J.A. 2001. Continuity conditions for a fault consisting of obliquely aligned cracks. *Geophysical Journal International* **144**, 679–684.

Tsvankin I. 1997a. Reflection moveout and parameter estimation for horizontal transverse isotropy. *Geophysics* **62**, 614–629.

Tsvankin I. 1997b. Anisotropic parameters and P-wave velocity for orthorhombic media. *Geophysics* **62**, 1292–1309.

Tsvankin I. 2001. *Seismic signatures and analysis of reflection data in anisotropic media.* Elsevier Science.

FIGURES

Figure 1. Pure-mode NMO ellipses computed from the exact equations (54) and (55) for a homogeneous horizontal layer containing a vertical fracture system. The background parameters and fracture weaknesses are $V_{Pb} = 2$ km/s, $V_{Sb} = 1$ km/s, $\rho = 2$ g/cm^3, $\Delta_N = 0.50$, $\Delta_V = \Delta_H = 0.25$, $\Delta_{NV} = \Delta_{NH} = \Delta_{VH} = 0.05$. The thin outside circle corresponds to a velocity of 2 km/s. The numbers around the circle indicate the azimuth α (in degrees) with respect to the fracture normal (i.e., the azimuth of the fracture strike is $\alpha = 90^\circ$).

Figure 2. Contours of the exact P-wave slowness surface $q(p_1, p_2)$ for the fractured model specified in Fig. 1.

Figure 3. Intersection of the slowness surface $q(p_1, p_2)$ in Fig. 2 with the vertical plane $p_2 = 0$.

Figure 4. Inversion of the vertical velocities and NMO ellipses of P-, S_1- and S_2-waves for the fracture and background parameters. The dots mark the correct values (see the caption of Fig. 1), the error bars correspond to the 95% confidence intervals in the estimated quantities. The relative error in the background P- and S-wave velocities (not shown) is smaller than that in g_b.

Figure 5. Same as Fig. 4 but for a model with the parameters $V_{Pb} = 2$ km/s, $V_{Sb} = 1$ km/s, $\rho = 2$ g/cm^3, $\Delta_N = \Delta_{NV} = \Delta_{VH} = 0.03$, $\Delta_V = \Delta_H = 0.40$, and $\Delta_{NH} = 0.07$. The eigenvalues $\Lambda_1 = 0.0$, $\Lambda_2 = 0.33$ and $\Lambda_3 = 0.34$ of the compliance matrix (4) correspond to fluid-filled fractures.

Figure 6. Inversion of the P-wave slowness surface (the range of the horizontal slownesses is given in Fig. 2) for the weaknesses Δ_{NV} and Δ_{VH}. The other model

parameters are fixed at the values shown in Fig. 4.

Figure 7. Same as Fig. 6 but for the model with fluid-filled fractures from Fig. 5.

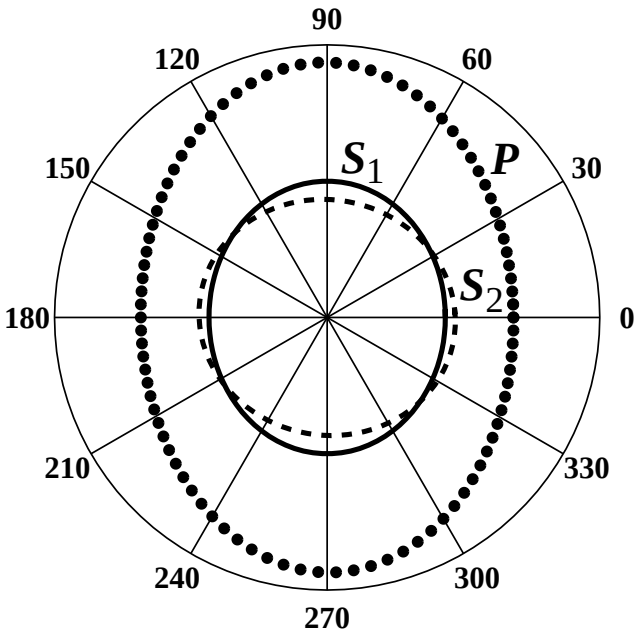

Figure 1. Pure-mode NMO ellipses computed from the exact equations (54) and (55) for a homogeneous horizontal layer containing a vertical fracture system. The background parameters and fracture weaknesses are $V_{Pb} = 2$ km/s, $V_{Sb} = 1$ km/s, $\rho = 2$ g/cm^3, $\Delta_N = 0.50$, $\Delta_V = \Delta_H = 0.25$, $\Delta_{NV} = \Delta_{NH} = \Delta_{VH} = 0.05$. The thin outside circle corresponds to a velocity of 2 km/s. The numbers around the circle indicate the azimuth α (in degrees) with respect to the fracture normal (i.e., the azimuth of the fracture strike is $\alpha = 90^\circ$).

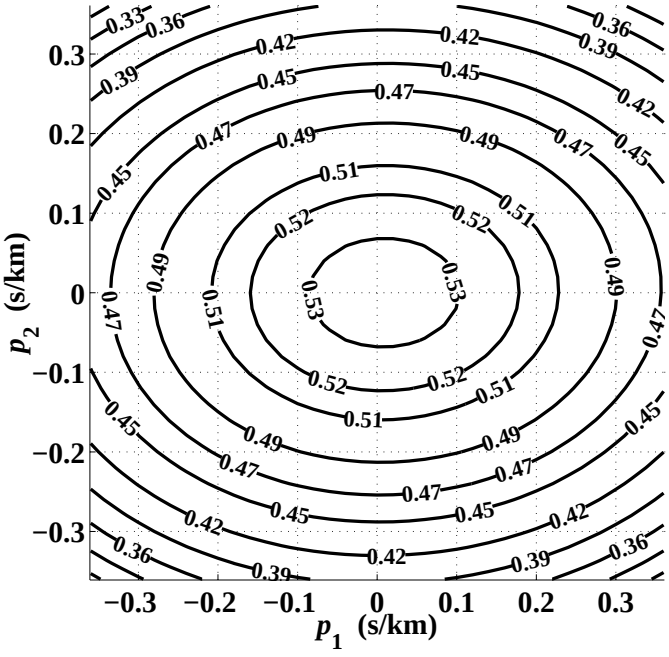

Figure 2. Contours of the exact P-wave slowness surface $q(p_1, p_2)$ for the fractured model specified in Fig. 1.

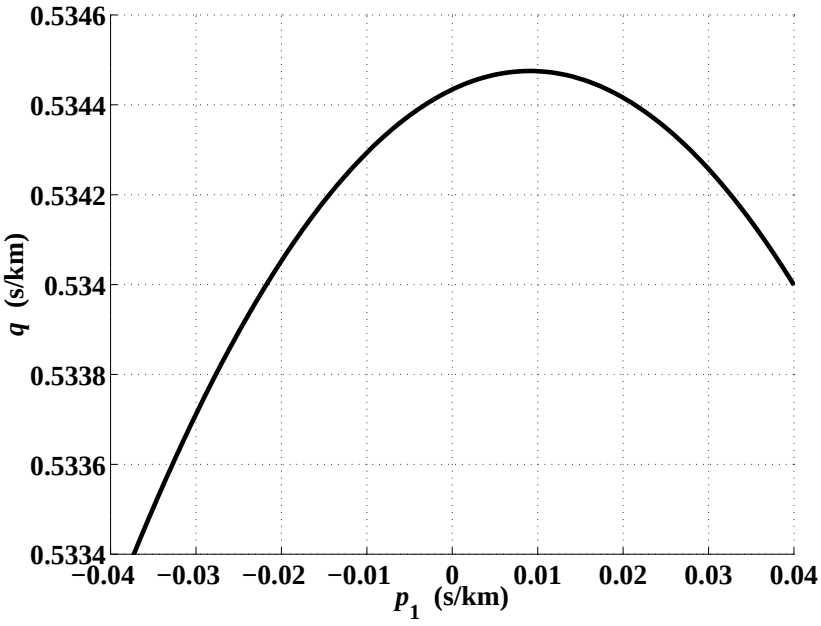

Figure 3. Intersection of the slowness surface $q(p_1, p_2)$ in Fig. 2 with the vertical plane $p_2 = 0$.

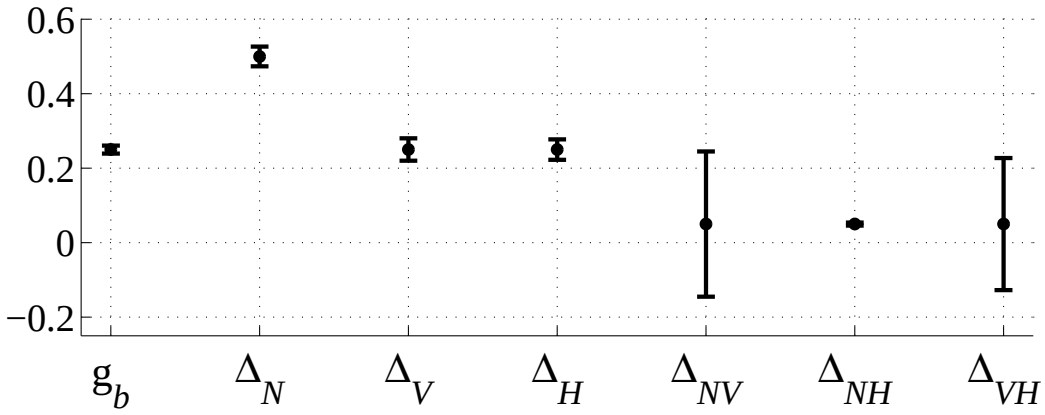

Figure 4. Inversion of the vertical velocities and NMO ellipses of P-, S_1- and S_2-waves for the fracture and background parameters. The dots mark the correct values (see the caption of Fig. 1), the error bars correspond to the 95% confidence intervals in the estimated quantities. The relative error in the background P- and S-wave velocities (not shown) is smaller than that in g_b.

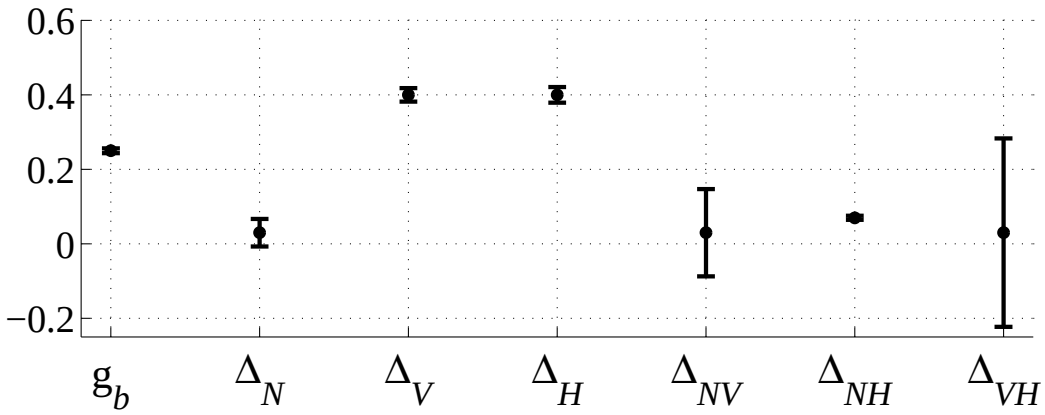

Figure 5. Same as Fig. 4 but for a model with the parameters $V_{Pb} = 2$ km/s, $V_{Sb} = 1$ km/s, $\rho = 2$ g/cm^3, $\Delta_N = \Delta_{NV} = \Delta_{VH} = 0.03$, $\Delta_V = \Delta_H = 0.40$, and $\Delta_{NH} = 0.07$. The eigenvalues $\Lambda_1 = 0.0$, $\Lambda_2 = 0.33$ and $\Lambda_3 = 0.34$ of the compliance matrix (4) correspond to fluid-filled fractures.

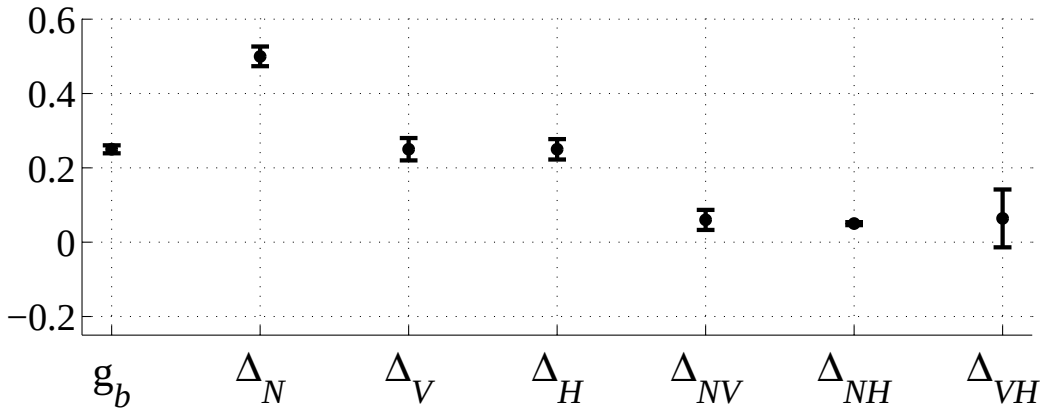

Figure 6. Inversion of the P-wave slowness surface (the range of the horizontal slownesses is given in Fig. 2) for the weaknesses Δ_{NV} and Δ_{VH}. The other model parameters are fixed at the values shown in Fig. 4.

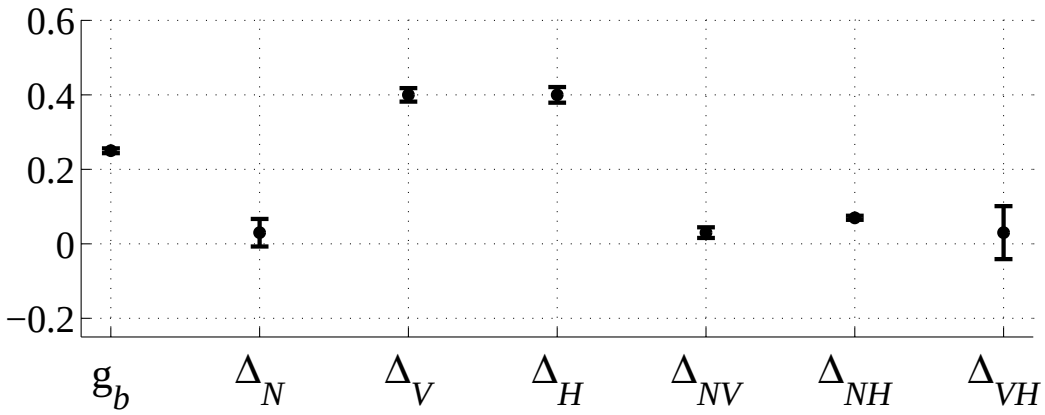

Figure 7. Same as Fig. 6 but for the model with fluid-filled fractures from Fig. 5.